

Excitation and detection of coherent magnon polarons in a ferromagnetic nanograting

Felix Godejohann,¹ Alexey V. Scherbakov,^{1,2} Serhii M. Kukhtaruk,^{1,3} Alexander N. Poddubny,² Dmytro D. Yaremkevich,¹ Mu Wang,⁴ Achim Nadzeyka,⁵ Dmitri R. Yakovlev,¹ Andrew W. Rushforth,⁴ Andrey V. Akimov,⁴ and Manfred Bayer¹

¹*Experimentelle Physik 2, Technische Universität Dortmund,
Otto-Hahn-Str. 4a, 44227 Dortmund, Germany.*

²*Ioffe Institute, Politechnicheskaya 26, 194021 St. Petersburg, Russia.*

³*Department of Theoretical Physics,
V.E. Lashkaryov Institute of Semiconductor Physics,
Pr. Nauky 41, 03028 Kyiv, Ukraine.*

⁴*School of Physics and Astronomy, University of Nottingham,
Nottingham NG7 2RD, United Kingdom.*

⁵*Raith GmbH, Konrad-Adenauer-Allee 8, 44263 Dortmund, Germany.*

Abstract

Strong coupling between two quanta of different excitations leads to the formation of a hybridized state which paves a way for exploiting new degrees of freedom to control phenomena with high efficiency and precision. A magnon polaron is the hybridized state of phonon and magnon, the elementary quanta of lattice vibrations and spin waves in a magnetically-ordered material. A magnon polaron can be formed at the intersection of the magnon and phonon dispersions, where their frequencies coincide. The observation of coherent magnon polarons in the time domain has remained extremely challenging because the weak interaction of magnons and phonons and their short lifetime jeopardize the strong coupling required for the formation of a hybridized state. Here, we overcome these limitations by localizing magnons and phonons in a nanograting fabricated from a metallic ferromagnet. The spatial matching of the localized phonon and magnon modes results in high coupling strength, which in combination with their long lifetime allow us to find clear evidence of an optically excited magnon polaron in the magnetic and elastic coherent responses of the nanograting. We show that the symmetries of the localized magnon and phonon states play a crucial role in the magnon polaron formation.

I. INTRODUCTION

Magnons are collective spin excitations in magnetically-ordered materials. Nowadays the manipulation of coherent high-frequency magnons on the nanoscale is one of the most prospective concepts for information technologies, also in the quantum regime. In this respect, the hybridization of magnons with phonons has been considered as a powerful method for spin control [1–7]. The magnon-phonon hybridization phenomenon in bulk materials is well understood [8, 9] and has been realized experimentally in the MHz frequency range [10]. However, on the nanoscale, where magnon and phonon frequencies reach the GHz and sub-THz frequency ranges, magnon-phonon hybridized states, referred to further as magnon polarons, are not yet comprehensively understood or utilized. Fundamental studies of magnon polaron properties in magnetic nanostructures can significantly enrich ultrafast methods for the generation, detection and manipulation of spin on the nanoscale [11–14].

Within last decade the magnon-phonon interaction has been actively studied in experiments with high-frequency coherent magnons and phonons [15–24]. For instance, the excitation of coherent magnons has been realized by broadband coherent phonon wavepackets [15, 17, 23, 24], localized monochromatic phonons [18, 19, 21, 22] and propagating surface acoustic waves [16, 20]. However, these experiments demonstrate only the one-way process of transferring energy from phonons to magnons with no evidence of strong coupling, characterized by a reversible energy exchange between them.

Direct evidence of the formation of magnon polarons would be an avoided crossing of the magnon and phonon dispersion curves at their intersection [8, 9]. A spectral gap around the magnon-phonon resonance clearly indicates strong coupling of two excitations with the formation of a hybridized state [25, 26]. Experimental observation of the avoided crossing for magnons and phonons is possible when the energy splitting at their resonance exceeds the spectral broadening of the interacting phonon and magnon modes. Only recently, experiments with Ni nanomagnets [27] have demonstrated that these conditions can be approached.

Here, we report experiments on the generation and detection of coherent magnon polarons in a metallic ferromagnetic nanograting (NG). We observe the *avoided crossing* effect as a result of magnon-phonon hybridization by detecting the transient magnon evolution excited by a femtosecond optical pulse and the respective spectrum. We demonstrate scenarios in which coherent magnon polarons can be generated by optical pulses and detected depending

on the spatial symmetry of the phonon and magnon eigenmodes of the nanostructure and on the initial and boundary conditions of the coupled system.

II. GALFENOL NANOGRATING AND LOCALIZED PHONON MODES

In the experiments, we use a magnetostrictive alloy of iron and gallium ($\text{Fe}_{0.81}\text{Ga}_{0.19}$), known as Galfenol, grown on GaAs substrate. This metal possesses both enhanced magnon-phonon interaction [28] and well-defined magnon resonances [29, 30]. By lateral nanoscale patterning of a thin Galfenol film, we achieve coherent phonon lifetimes of several nanoseconds at room temperature, which results in the formation of localized phonon modes with high Q-factors. Figure 1a illustrates the structure studied and the experimental scheme based on a conventional magneto-optical pump-probe technique (see the Methods section for details). The pump pulse which excites coherent phonons and magnons from the substrate side has 150 fs duration and is focused to a spot of 5 microns diameter with an excitation energy density of 12 mJ/cm^2 . The linearly polarized probe pulse is focused to a spot of 1 micron diameter at the NG front side opposite to the pump spot. By measuring the intensity of the reflected probe pulse, $\Delta I(t)$, where t is the time delay between the probe and pump pulses, we monitor the coherent photoelastic response of the NG [31]. To measure the time evolution of the magnetization, we use a detection scheme which monitors the polar Kerr rotation (KR) of the probe pulse polarization plane, $\Psi(t)$ [32]. An external magnetic field, B , applied in the NG plane along the [110]-axis of GaAs (the NG diagonal), serves to control the precession (magnon) spectrum.

The phonon spectrum generated by the pump pulse includes several phonon modes localized in the NG. These modes are excited due to the strong absorption (20 nm penetration depth) of the pump pulse in Galfenol. The calculated spatial profiles of the atom displacements corresponding to the localized modes are shown in Fig. 1b. Both modes are standing pseudo-surface acoustic waves [33], which possess two displacement components along the x - and z -axis. Therefore, they are characterized by three components of the dynamical strain: η_{xx} , η_{zz} , η_{xz} . The mode shown in the lower panel of Fig. 1b is a Rayleigh-like standing wave with dominant displacement along the z -axis, i.e. perpendicular to the NG plane. We refer to this mode as a quasi-transverse acoustic (QTA) mode. It is important to mention that there is a counterpart of the QTA mode, which has different symmetry properties and

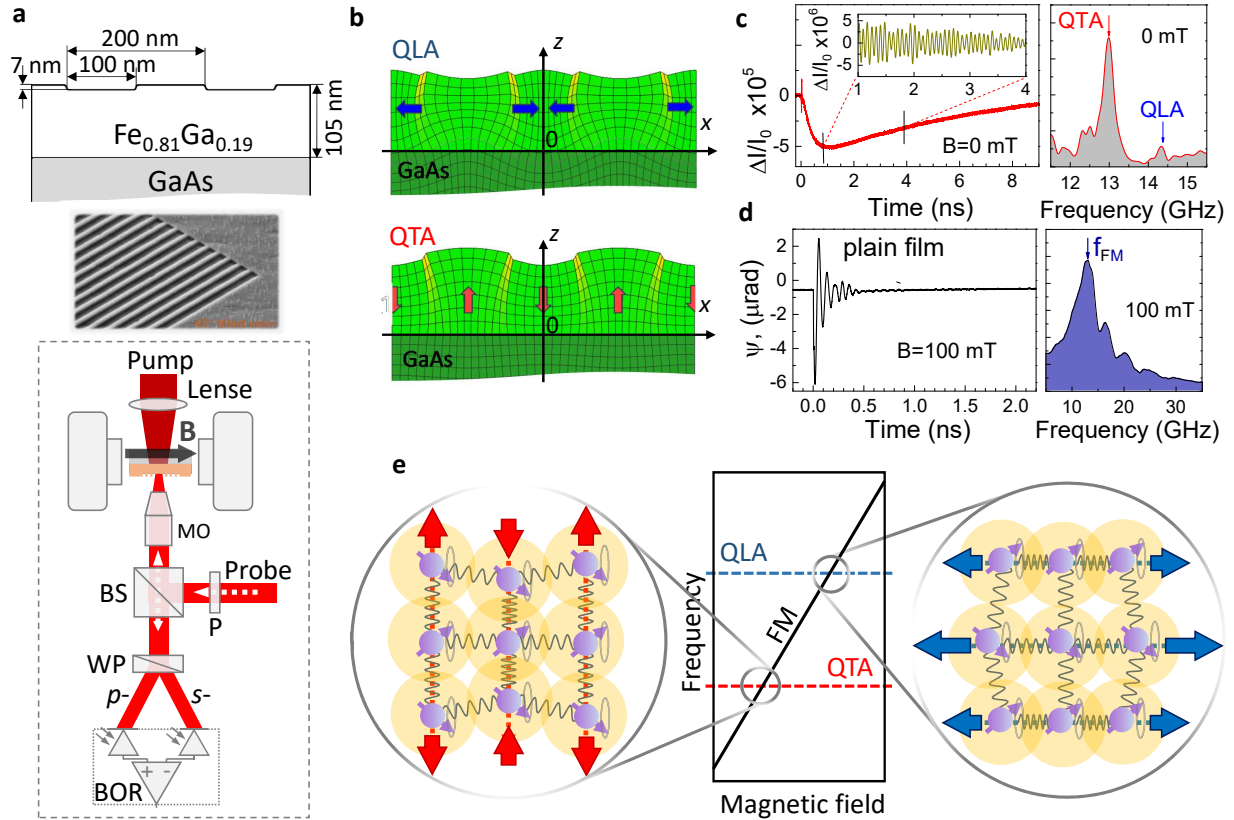


Figure 1. Phonons and magnons in a Gallenol nanograting. **a** Design of the studied sample, its SEM image, and the experimental scheme: MO – microobjective, WP – Wollaston prism, BOR – balanced optical receiver, BS – beam splitter, P - polariser. **b** Calculated displacements for two phonon modes excited by the pump pulse. Black arrows illustrate the used coordinate system. **c** Transient reflectivity signal and its fast Fourier transform (FFT). The inset shows the close-up of the transient signal after subtraction of the slow background. **d** Transient Kerr rotation signal measured from an unpatterned part of the studied film and its FFT. **e** A diagram, which demonstrates the idea of the experiment: the field-dependent magnon mode (oblique line) is tuned into resonance with the field-independent phonon modes (horizontal lines) by an external magnetic field. The crossing points correspond to the FM-QTA and FM-QLA resonance conditions where the magnon-phonon hybridization is expected.

cannot be excited optically. This localized mode is almost degenerate with the QTA mode, but as we show below, can play a crucial role in the interactions with magnons.

Another mode, shown in the top panel of Fig. 1b is often referred to as a surface skimmed longitudinal mode [21]. It has a predominant in-plane displacement and we refer to this mode as a quasi-longitudinal acoustic (QLA) mode. The calculated frequencies [see the Methods section and Supplementary Note 1] of the QTA and QLA modes are 13.1 and 15.3 GHz, respectively. The QTA and QLA modes are excited simultaneously and are expected to have similar amplitudes and lifetimes of 3.5 ns with a corresponding Q-factor of about 100.

However, due to the specific polarization and spatial distribution, the QLA mode provides a significantly smaller contribution to the reflectivity signal [for details of calculations see Supplementary Note 1]. This can be seen in $\Delta I(t)$ and its fast Fourier transform (FFT) shown in Fig. 1c, where the lower spectral line at $f_{\text{QTA}} = 13.0$ GHz has a large amplitude, while the upper, QLA mode, is less visible at $f_{\text{QLA}} = 14.5$ GHz. A small low frequency shift of the measured frequencies relative to the calculated ones is due to minor structural uncertainties and a moderate heating of the film under illumination by the pump and probe pulses.

III. MAGNON SPECTRUM OF THE NANOGRATING AND THE EXPERIMENTAL CONCEPT

Now we consider the magnon spectrum of the NG. The studied grating is formed by shallow grooves, the depth of which are much smaller than the grating period and the ferromagnetic film thickness. In this case, the magnon spectrum is close to that of an unpatterned film [34]. The transient KR signal measured for a plain Galfenol film (outside the NG) and its FFT are shown in Fig. 1d. The fast decaying oscillations in the transient KR signal reflect the magnetization precession excited by the femtosecond optical pulse [35, 36]. The broad magnon spectrum shows several peaks, which correspond to the standing magnon modes quantized along the z -axis [30, 35]. The fundamental magnon (FM) mode with the lowest frequency of 13.0 GHz for $B = 100$ mT is dominant in the spectrum. In the NG, the magnon modes possess additional spatial modulation along the x -axis with the NG period d due to the periodically modulated demagnetizing field (shape anisotropy) given by the NG spatial profile [34]. Despite the modulation along the x -direction, the FM mode remains the most pronounced in the magnon spectrum of the NG and possesses a similar dependence of the spectral position on B as in the plain Galfenol film [34]. The main object of our study is the interaction of this FM mode with the two localized phonon modes, QTA and QLA.

The idea of our experiments is demonstrated schematically in Fig. 1e, which shows the predicted magnetic field dependences of the frequencies for uncoupled localized phonon and FM modes. For phonons, the frequencies are independent of B and are shown as horizontal lines. For the FM mode, the dependence on B is linear in a certain range of magnetic field. The magnon-phonon hybridization phenomena are expected at the crossing points.

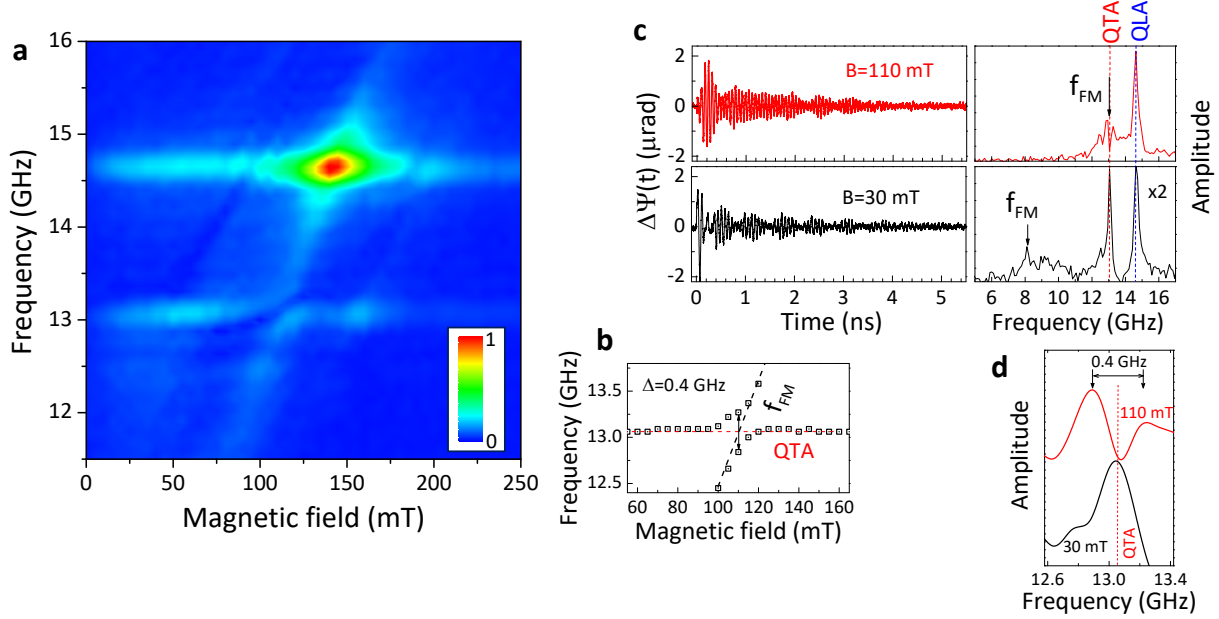


Figure 2. Hybridization of magnon and phonon modes. **a** Color map which shows the spectral density of the measured KR signal as a function of the external magnetic field. The anti-crossing is observed at $f = 13$ GHz and $B = 110$ mT. **b** Magnetic field dependence of the spectral peaks in the magnon spectrum around the intersection of the QTA and FM modes. **c** Measured temporal KR signals (left panels) and their FFTs (right panels) at non-resonant ($B = 30$ mT) and resonant ($B = 110$ mT) conditions. **d** Zoomed fragments of the FFT spectra shown in **c** around the resonance frequency. The splitting of the line in the resonance at $B = 110$ mT is clearly seen.

Experimentally, we measure the transient KR signals at various B . By analyzing the FFTs of the measured transient signals, we obtain information about the FM spectrum paying special attention to the resonance conditions.

IV. AVOIDED CROSSING AT THE MAGNON-PHONON RESONANCE

Figure 2 summarizes our main experimental observations. The color contour map in Fig. 2a shows the field dependence of the spectral density of the transient KR signal. The pivotal result is the well-resolved avoided crossing effect observed at the resonant conditions where $B = 110$ mT. The spectral splitting around the intersection of the FM and QTA modes, Δ , can be quantified as $\Delta = 0.4$ GHz. The presence of the avoided crossing and the value of Δ are demonstrated also in Fig. 2b, which shows the dependences of the frequencies for the two spectral peaks around 13.0 GHz in the measured FFT spectra. Figure 2c shows the measured temporal KR signals and their spectra obtained for non-resonant ($B = 30$ mT) and

resonant ($B = 110$ mT) conditions. For non-resonant conditions the spectrum consists of a broad magnon band which includes a peak at f_{FM} corresponding to the FM mode and two intense narrow peaks at the frequencies of the QTA and QLA phonon modes. The existence and high amplitudes of these two peaks are due to the driving of high-order magnon modes in the NG by the localized QTA and QLA phonon modes [36]. For the resonance conditions where the frequency of the FM mode, f_{FM} , coincides with the frequency of the QTA phonon mode, f_{QTA} , the spectral splitting around $f = f_{\text{FM}} = f_{\text{QTA}}$ is observed (see also the zoomed fragments in Fig. 2d), which indicates the avoided crossing effect.

The observed avoided crossing is direct evidence of the hybridized magnon-phonon state, i.e. the magnon polaron. Besides the avoided crossing there are several other experimental observations, which require further understanding:

- (i) The first this concerns the resonance of the FM mode with the QLA mode evidently seen as a bright red spot in Fig. 2a at $B = 140$ mT. It is interesting that the dependencies of the amplitudes of the KR signals at the QTA ($B = 110$ mT) and QLA ($B = 140$ mT) resonances are very different. Figure 3a shows the temporal KR signal and its FFT measured at $B = 140$ mT, when the frequencies of the FM and QLA modes coincide, $f_{\text{FM}} = f_{\text{QLA}}$. The strong increase of the spectral amplitude at the frequency of the QLA mode, which becomes five times larger than out of resonance (see Fig. 3b), is clearly seen. This obviously points towards resonant driving of the FM mode by the QLA mode [19, 22, 23, 37]. In contrast, no increase of the spectral amplitude of the FM mode at the resonance with the QTA mode, $f_{\text{FM}} = f_{\text{QTA}}$, is observed.
- (ii) Secondly, despite the effective phonon driving, the spectral gap, which manifests the avoided crossing, is not detected at the resonance of the FM mode and the QLA mode around $B = 140$ mT.

Thus, at a glance, there are two qualitative differences in the behavior of the FM-QTA and FM-QLA resonances. (i) If the interaction between the optically excited localized phonon mode and the magnon mode is strong enough for their hybridization, this should result in strong phonon driving of magnons at the resonant conditions [19, 22, 23, 37]. However, this does not happen for the FM-QTA resonance. Instead, it shows an avoided crossing. (ii)

The effective resonant phonon driving suggests that the FM-QLA interaction has nonzero coupling strength, but the spectral gap due to the avoided crossing effect is not detected experimentally for this resonance.

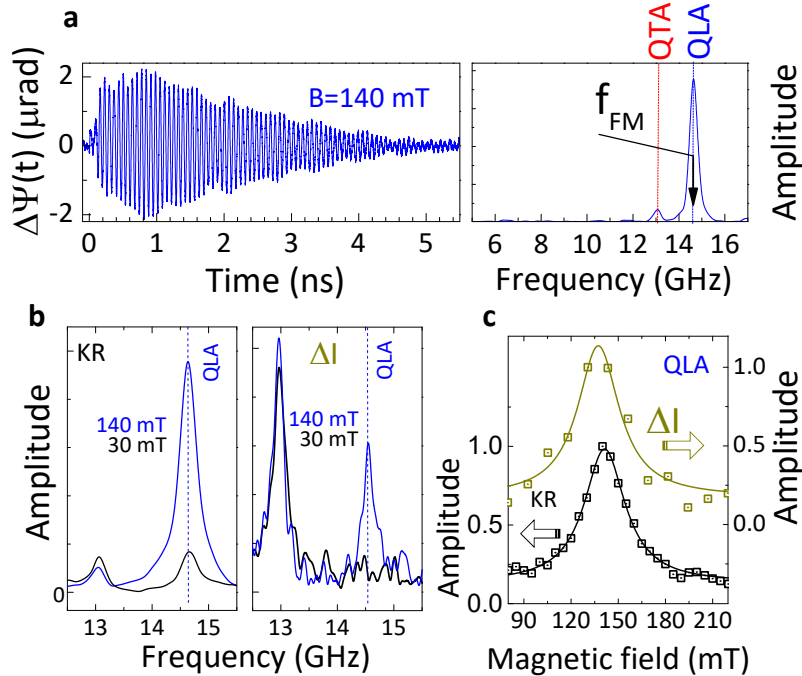


Figure 3. Phonon driving of magnons. **a** Kerr rotation signal and its FFT measured at $B = 140$ mT corresponding to the resonance of the FM and QLA phonon modes. **b** FFTs around f_{QLA} obtained from the KR (left panel) and reflectivity (right panel) signals measured at resonant ($B = 140$ mT) and non-resonant ($B = 30$ mT) conditions. **c** Magnetic field dependencies of the normalized amplitudes at $f = f_{\text{QLA}} = 14.5$ GHz for the Kerr rotation (lower) and reflectivity (upper) signals. Lines are guides for the eye.

V. SYMMETRIES OF THE MODES AND A MODEL OF COUPLED OSCILLATORS

To understand the differences in the manifestations of the two magnon-phonon resonances, we analyze the magnon-phonon interaction in the NG in more detail. Our analysis is based upon the approach developed in Ref. [38]. It has been shown that the coupling strength of interacting magnon and phonon modes can be determined by the spatial overlap of the dynamical magnetization, $\delta\mathbf{m}$, of a magnon mode and the strain components of a phonon mode. In this case, the interacting magnon and phonon modes can be considered as two coupled oscillators [38]. Due to the in-plane orientation of the external magnetic field

the z -component of steady-state magnetization can be assumed to be zero. In this case, for modeling the magnon-phonon interaction we may consider only two strain components: η_{xx} and η_{xz} [37]. The coupling strength, $\kappa = \Delta/2$, for the magnon and phonon modes at resonance is defined by two overlap integrals:

$$\kappa = \beta_1 \int \tilde{\eta}_{xx} \delta \tilde{m}_x dV + \beta_2 \int \tilde{\eta}_{xz} \delta \tilde{m}_z dV, \quad (1)$$

where $\delta \tilde{m}_{x,z}$ and $\tilde{\eta}_{xx,xz}$ are the projections of the dynamical magnetization of the magnon mode and the strain components of the phonon mode, respectively, normalized in such a way that $\int \delta \tilde{m}_{x,z}^2 dV = \int \tilde{\eta}_{xx,xz}^2 dV = 1$ (dV is a unit volume element). The coefficients β_1 and β_2 , which have dimension of frequency, are defined by the material parameters including the magneto-elastic coefficients, the saturation magnetization M_s , the mass density of the media, as well as the external magnetic field orientation and the resonant frequency [39].

To evaluate Eq. 1 we consider the spatial distribution of the phonon modes localized in the NG. As mentioned earlier, there is a counterpart of the QTA mode referred to as QTA*. The spatial distributions of the strain components are shown in the bottom of Fig. 4a. The frequency splitting of the QTA and QTA* modes is ≈ 0.1 GHz, which is less than their spectral width. Thus, they may be considered as degenerate. The only difference between the QTA and QTA* mode is the symmetry along the x -axis. We refer to the QTA mode as symmetric due to the symmetry of the strain components $\tilde{\eta}_{xx}$ and $\tilde{\eta}_{zz}$ relative to the center of the groove of the NG. The QTA* mode is referred to as antisymmetric. Only the QTA mode is excited by the pump pulse (see Supplementary Note 1). The QTA* mode cannot be excited by the pump pulse due to the antisymmetric nature of $\tilde{\eta}_{zz}$, and it also cannot be optically detected. However, the other strain component $\tilde{\eta}_{xz}$, has the opposite symmetry which will be important for the interaction with magnons: it is antisymmetric for QTA and symmetric for QTA*.

Next, we consider the magnon spatial distribution, assuming mixed boundary conditions for the magnetization in the studied structure along the z -axis: pinning at the (Fe,Ga)/GaAs interface and free precession at the patterned surface of the NG [40]. Then, the spatial distribution of the normalized dynamical magnetization, $\delta \tilde{\mathbf{m}}$, for the FM mode can be written as

$$\delta \tilde{m}_x = \delta \tilde{m}_z = A \cos\left(\frac{2\pi}{d}x\right) \sin\left(\frac{\pi}{2h}z\right), \quad (2)$$

where $z = 0$ corresponds to the (Fe,Ga)/GaAs interface. The spatial distribution of $\delta\tilde{\mathbf{m}}$ is shown in the center of Fig. 4a. The calculations based on Eqs. 1 and 2 show that the overlaps of the FM mode distribution with both $\tilde{\eta}_{xx}$ and $\tilde{\eta}_{xz}$ for the QTA mode are negligible due to their poor spatial match: the overlap integrals for both strain components are less than 10^{-3} . In contrast, the FM mode closely matches the $\tilde{\eta}_{xz}$ of the antisymmetric QTA* mode, which leads to the coupling strength $\kappa_{\text{QTA}^*} \approx 0.77\beta_2$. Thus, the coupling strength of the FM mode for the QTA* mode is three orders of magnitude stronger than for the QTA mode in the NG. We conclude that the experimentally observed hybridization corresponds to the coupling of the FM with the antisymmetric QTA* mode. The magnon polaron is excited via the excitation of the FM mode by the optical pump pulse and detected by the probe pulse in the KR signal, also via the FM mode. The phonon QTA* mode is not excited optically and, therefore, driving of the FM mode by the QTA* mode does not take place, which agrees with the experimental observation for the lower magnon-phonon resonance at $B = 110$ mT. This explains the experimental observation of the avoided crossing effect without resonant driving by phonons, as demonstrated in Fig. 2. The value of the measured spectral splitting $\Delta = 0.4$ GHz at the resonance is close to the calculated value of $\Delta = 0.27$ GHz for the frequency splitting of a pure transverse wave propagating in bulk Gallenol in the same experimental geometry (Supplementary Note 2).

A similar analysis for the QLA mode, for which the spatial distribution is demonstrated in the upper part of Fig. 4a, shows that the spatial overlap of the FM mode with the optically excited QLA mode is large: $\kappa_{\text{QLA}} = 0.98\beta_1$ and driving of the FM mode by the QLA mode should take place. This agrees with the experimental results shown in Fig. 3c where the increase of the KR signal at the resonance is clearly seen. However, the spectral gap due to the avoided crossing is not observed for this resonance in Fig. 2a. A simple explanation could be a small value of β_1 and respectively a weak coupling of the QLA and FM modes. Then, the magnon-phonon interaction would not be accompanied by the modification of the magnon spectrum and only the resonant phonon driving of the magnon mode would take place [19, 22, 23, 37]. However, the formation of the magnon polaron may still take place, but the avoided crossing would be masked by the energy transfer from the phonon mode. This will happen in the case of a coupling with a cooperativity $C = \kappa^2/(\gamma_p\gamma_m) \approx 1$, where γ_p and γ_m are the damping rates of the phonon and magnon modes, respectively. To show this, we analyze a model of three coupled harmonic oscillators [38] (the system of equations

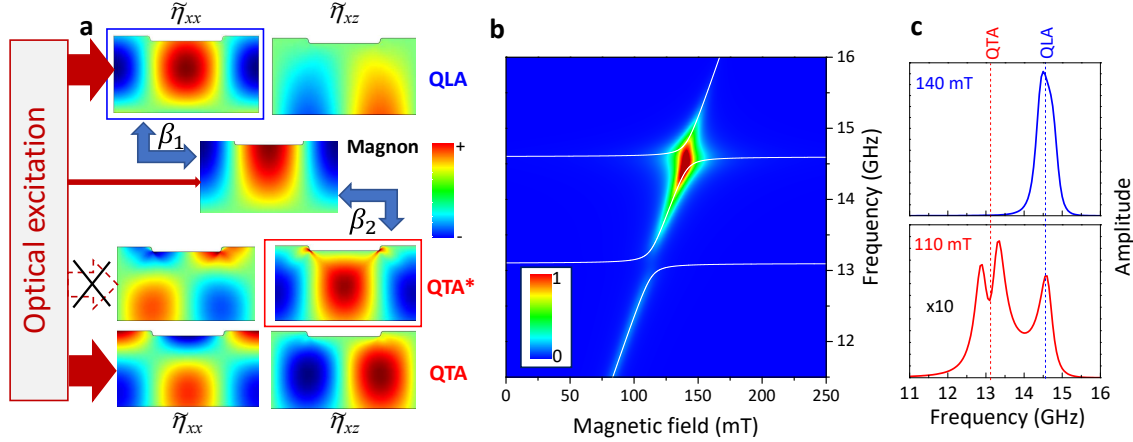


Figure 4. Modeling of the magnon polaron spectrum. **a** Spatial distributions of the normalized dynamical magnetization of the fundamental magnon mode and the normalized strain components for the symmetric QTA, antisymmetric QTA* and symmetric QLA modes. The blue arrows show the pairs, for which the overlap integrals have non-negligible values. **b** The colour map shows the calculated magnetic field dependence of the spectral density of the magnon states calculated in the model of three coupled harmonic oscillators. The initial conditions for the calculations are set as following: the lower QTA* mode is not excited (as mentioned in the text), the energy transfer from the pump pulse to the upper QLA mode significantly exceeds the energy transferred to the FM mode. **c** Calculated magnon spectra for magnetic fields corresponding to the resonance of the FM mode with the QTA mode ($B = 110$ mT) and with the QLA mode ($B = 140$ mT).

and parameters used for the calculations can be found in the Methods section). The result, shown in Fig. 4b shows strong similarities with the experimental color map in Fig. 2, so that the model can be considered as prototypical for the involved physics. In the calculations, the spectral width of all the oscillators is 0.2 GHz and the coupling strength of the lower (QTA*) and upper (QLA) resonances with the field dependent one (FM) corresponds to the frequency splitting $\Delta = 0.4$ GHz ($\kappa = 0.2$ GHz). The results are shown for the initial conditions when the QTA* mode is not excited and the energy transferred from the optical pump pulse to the QLA mode is 100 times higher than the energy injected into the FM mode. The main features of the magnon spectra in the calculated color map of Fig. 4b, i.e. the avoided crossing and the driving, are in qualitative agreement with the experimentally measured magnon spectra shown in Fig. 2a. Indeed, the avoided crossing effect is observed for the lower FM-QTA* resonance mode while for the upper FM-QLA resonance the splitting of the hybridized state is masked by strong driving of the FM mode by resonant phonons. It is worth mentioning, that if the same coupled modes are excited with equal initial amplitudes an avoided crossing is well resolved (Supplementary Note 3).

VI. MAGNON POLARON IN THE REFLECTIVITY SIGNAL

To make conclusions about the interaction of magnons with the QLA mode we discuss the experimental reflectivity signals, $\Delta I(t)$, governed by the amplitudes of the QTA and QLA modes. The spectral amplitude of the QTA mode in the reflectivity signal does not depend strongly on B , which agrees with our model where the lower QTA mode does not interact with the FM mode. The contribution of the upper QLA mode to $\Delta I(t)$ out of resonance is quite weak, which is apparently due to an inefficient photo-elastic effect. However, in contrast to the QTA mode, $\Delta I(t)$ for the QLA mode significantly increases at the FM-QLA resonance of $B = 140$ mT as demonstrated in the right panel in Fig. 3b and Fig. 3c. Such an increase can be due to the formation of magnon polarons at the magnon-QLA phonon resonance. Indeed, at the resonance the polarization of a phonon mode is distorted by a magnon mode similarly to how it happens in the bulk [41] and for surface acoustic waves [42]. The in-plane shear component makes the QLA mode visible in the photo-elastic effect (see Supplementary Note 1). In this case, the reflectivity signal, $\Delta I(t)$, for the QLA mode increases at the resonance field ($B = 140$ mT), which is observed in our experiment. This explanation supports the assumption about the formation of a magnon polaron at the QLA resonance. However, the influence of quadratic magneto-optical Kerr effects on the reflectivity signal at the resonance conditions, when the precession amplitude is large, cannot be fully excluded [43].

VII. CONCLUSIONS

To conclude, we have studied experimentally the properties of localized magnon-phonon hybrid excitations in a ferromagnetic nanograting. By changing the external magnetic field we are able to realize resonance conditions for a magnon mode with two localized phonon modes with different polarizations. At the resonance with the lower phonon mode we observed a frequency splitting which points to the excitation of a hybridized state, i.e. a magnon polaron. At the resonance with the upper phonon mode we observe a strong driving of the magnon mode by the phonon mode without detecting any frequency splitting. We explain the experimental observations by analyzing the calculated spatial profiles of the phonon modes and show the crucial roles of the phonon mode symmetry and the initial

excitation conditions of the magnon polaron by the optical pump pulse.

Direct observation of magnon polarons in the time domain paves the way for exploiting new degrees of freedom for spin excitation and for the manipulation of spins at the nanoscale. Magnon polarons allow control of spins via phonons: for instance, magnon polarons may be excited and detected via coherent phonons when direct spin excitation cannot be efficiently achieved by microwave or optical techniques. Magnon-phonon hybridization broadens the possibilities to control spin pumping [7] and the Seebeck effect [2]. The existence of magnon polarons results in a gap in the magnon spectrum that can help to localize magnetic excitations due to phonon localization on a defect in a periodic nanostructure. Magnon polarons should play an important role in spin-spin interactions and the related phenomenon of magnon Bose-Einstein condensation [3]. An appealing prospect is to use the long coherence times and tunability of magnon polarons for creating states with defined magnon polaron numbers, thus providing new routes for quantum information and metrology [44].

-
- [1] Weiler, M. *et al.* Spin pumping with coherent elastic waves. *Phys. Rev. Lett.* **108**, 176601 (2012).
 - [2] Kikkawa, T. *et al.* Magnon polarons in the spin Seebeck effect. *Phys. Rev. Lett.* **117**, 207203 (2016).
 - [3] Bozhko, D. A. *et al.* Bottleneck accumulation of hybrid magnetoelastic bosons. *Phys. Rev. Lett.* **118**, 237201 (2017).
 - [4] Man, H. *et al.* Direct observation of magnon-phonon coupling in yttrium iron garnet. *Phys. Rev. B* **96**, 100406(R) (2017).
 - [5] Cornelissen, L. J. *et al.* Nonlocal magnon-polaron transport in yttrium iron garnet. *Phys. Rev. B* **96**, 104441 (2017).
 - [6] Holanda, J., Maior, D. S., Azevedo, A. & Rezende, S. M. Detecting the phonon spin in magnon-phonon conversion experiments. *Nat. Phys.* **14**, 500–506 (2018).
 - [7] Hayashi, H. & Ando, K. Spin pumping driven by magnon polarons. *Phys. Rev. Lett.* **121**, 237202 (2018).
 - [8] Kittel, C. Interaction of spin waves and ultrasonic waves in ferromagnetic crystals. *Phys. Rev.* **110**, 836–841 (1958).

- [9] Akhiezer, A., Bar'iakhtar, V. & Peletminskii, S. Coupled magnetoelastic waves in ferromagnetic media and ferroacoustic resonance. *Sov. Phys. JETP* **35**, 157–164 (1959).
- [10] Belyaeva, O. Y., Karpachev, S. N. & Zarembo, L. K. Magnetoacoustics of ferrites and magnetoacoustic resonance. *Sov. Phys. Uspekhi* **35**, 106–122 (1992).
- [11] Shen, K. & Bauer, G. E. W. Laser-induced spatiotemporal dynamics of magnetic films. *Phys. Rev. Lett.* **115**, 197201 (2015).
- [12] Kamra, A., Keshtgar, H., Yan, P. & Bauer, G. E. W. Coherent elastic excitation of spin waves. *Phys. Rev. B* **91**, 104409 (2015).
- [13] Graczyk, P. & Krawczyk, M. Coupled-mode theory for the interaction between acoustic waves and spin waves in magnonic-phononic crystals: Propagating magnetoelastic waves. *Phys. Rev. B* **96**, 024407 (2017).
- [14] Li, J., Zhu, S.-Y. & Agarwal, G. Magnon-photon-phonon entanglement in cavity magnomechanics. *Phys. Rev. Lett.* **121** (2018).
- [15] Scherbakov, A. V. *et al.* Coherent magnetization precession in ferromagnetic (Ga,Mn)As induced by picosecond acoustic pulses. *Phys. Rev. Lett.* **105**, 117204 (2010).
- [16] Weiler, M. *et al.* Elastically driven ferromagnetic resonance in nickel thin films. *Phys. Rev. Lett.* **106**, 117601 (2011).
- [17] Kim, J.-W., Vomir, M. & Bigot, J.-Y. Ultrafast magnetoacoustics in nickel films. *Phys. Rev. Lett.* **109**, 166601 (2012).
- [18] Afanasiev, D. *et al.* Laser excitation of lattice-driven anharmonic magnetization dynamics in dielectric FeBO₃. *Phys. Rev. Lett.* **112**, 147403 (2014).
- [19] Yahagi, Y., Harteneck, B., Cabrini, S. & Schmidt, H. Controlling nanomagnet magnetization dynamics via magnetoelastic coupling. *Phys. Rev. B* **90**, 140405(R) (2014).
- [20] Thevenard, L. *et al.* Surface-acoustic-wave-driven ferromagnetic resonance in (Ga,Mn)(As,P) epilayers. *Phys. Rev. B* **90**, 094401 (2014).
- [21] Janušonis, J., Chang, C. L., van Loosdrecht, P. H. M. & Tobey, R. I. Frequency tunable surface magneto elastic waves. *Appl. Phys. Lett.* **106**, 181601 (2015).
- [22] Jäger, J. V. *et al.* Resonant driving of magnetization precession in a ferromagnetic layer by coherent monochromatic phonons. *Phys. Rev. B* **92**, 020404(R) (2015).
- [23] Deb, M. *et al.* Picosecond acoustic-excitation-driven ultrafast magnetization dynamics in dielectric Bi-substituted yttrium iron garnet. *Phys. Rev. B* **98**, 174407 (2018).

- [24] Hashimoto, Y. *et al.* Frequency and wavenumber selective excitation of spin waves through coherent energy transfer from elastic waves. *Phys. Rev. B* **97**, 140404(R) (2018).
- [25] Novotny, L. Strong coupling, energy splitting, and level crossings: A classical perspective. *Am. J. Phys.* **78**, 1199–1202 (2010).
- [26] Rodriguez, S. R.-K. Classical and quantum distinctions between weak and strong coupling. *Eur. J. Phys.* **37**, 025802 (2016).
- [27] Berk, C. *et al.* Strongly coupled magnon–phonon dynamics in a single nanomagnet. *Nat. Commun.* **10**, 2652 (2019).
- [28] Atulasimha, J. & Flatau, A. B. A review of magnetostrictive iron–gallium alloys. *Smart Mat. Struct.* **20**, 043001 (2011).
- [29] Parkes, D. E. *et al.* Magnetostrictive thin films for microwave spintronics. *Sci. Reports* **3**, 2220 (2013).
- [30] Scherbakov, A. *et al.* Optical excitation of single- and multimode magnetization precession in Fe - Ga nanolayers. *Phys. Rev. Applied* **11**, 031003 (2019).
- [31] Thomsen, C., Grahn, H. T., Maris, H. J. & Tauc, J. Surface generation and detection of phonons by picosecond light pulses. *Phys. Rev. B* **34**, 4129–4138 (1986).
- [32] Hiebert, W. K., Stankiewicz, A. & Freeman, M. R. Direct observation of magnetic relaxation in a small permalloy disk by time-resolved scanning Kerr microscopy. *Phys. Rev. Lett.* **79**, 1134–1137 (1997).
- [33] Nardi, D. *et al.* Probing thermomechanics at the nanoscale: Impulsively excited pseudosurface acoustic waves in hypersonic phononic crystals. *Nano Lett.* **11**, 4126–4133 (2011).
- [34] Langer, M. *et al.* Spin-wave modes in transition from a thin film to a full magnonic crystal. *Phys. Rev. B* **99**, 024426 (2019).
- [35] van Kampen, M. *et al.* All-optical probe of coherent spin waves. *Phys. Rev. Lett.* **88**, 227201 (2002).
- [36] Kats, V. N. *et al.* Ultrafast changes of magnetic anisotropy driven by laser-generated coherent and noncoherent phonons in metallic films. *Phys. Rev. B* **93**, 214422 (2016).
- [37] Salasyuk, A. S. *et al.* Generation of a localized microwave magnetic field by coherent phonons in a ferromagnetic nanograting. *Phys. Rev. B* **97**, 060404(R) (2018).
- [38] Verba, R., Lisenkov, I., Krivorotov, I., Tiberkevich, V. & Slavin, A. Nonreciprocal surface acoustic waves in multilayers with magnetoelastic and interfacial Dzyaloshinskii-Moriya inter-

- actions. *Phys. Rev. Appl.* **9**, 064014 (2018).
- [39] For pure longitudinal and transverse acoustic waves in the bulk, β_1 and β_2 are determined by the respective magneto-elastic coefficients, b_1 and b_2 , and may be obtained analytically (Supplementary Note 2). However, for the phonon modes of mixed polarizations localized in the NG, β_1 and β_2 are determined by the combinations of b_1 and b_2 and can be calculated by means of numerical simulation. Thus, the following analysis is based on the values estimated from the experiment.
- [40] As it has been shown in Ref. [30] the magnon spectrum of a plain Gallferol film grown on a GaAs substrate and covered by a Cr layer, corresponds to the pinning boundary conditions for both interfaces. However, it is reasonable to suggest that in a patterned structure with the Cr cap removed (within and around the grooves), the open surface is characterized by a free boundary condition for the precessing magnetization.
- [41] Matthews, H. & LeCraw, R. C. Acoustic wave rotation by magnon-phonon interaction. *Phys. Rev. Lett.* **8**, 397–399 (1962).
- [42] Scott, R. Q. & Mills, D. L. Propagation of surface magnetoelastic waves on ferromagnetic crystal substrates. *Phys. Rev. B* **15**, 3545–3557 (1977).
- [43] Postava, K. *et al.* Linear and quadratic magneto-optical measurements of the spin reorientation in epitaxial Fe films on MgO. *Journal of Magnetism and Magnetic Materials* **172**, 199–208 (1997).
- [44] Chu, Y. *et al.* Creation and control of multi-phonon Fock states in a bulk acoustic-wave resonator. *Nature* **563**, 666–670 (2018).
- [45] Bartels, A. *et al.* Ultrafast time-domain spectroscopy based on high-speed asynchronous optical sampling. *Rev. Sci. Instrum.* **78**, 035107 (2007).
- [46] COMSOL Multiphysics[®] v. 5.4., <http://www.comsol.com>, COMSOL AB, Stockholm, Sweden.

VIII. METHODS

A. Sample growth and post-growth processing

A film of $\text{Fe}_{0.81}\text{Ga}_{0.19}$ of 105 nm thickness was epitaxially grown on a (001)-GaAs substrate after 10 periods of a GaAs/AlAs (59 nm/71 nm) superlattice. The Gallferol film was capped

by a 3-nm-thick Cr layer to prevent oxidation. The nanograting (NG) of $25 \times 25 \mu\text{m}^2$ size was formed by milling parallel grooves in the sample surface along the [100] crystallographic axis of the GaAs substrate using a focused beam of Ga ions (Raith VELION FIB-SEM). The grooves have depth $a = 7 \text{ nm}$ and width $w = 100 \text{ nm}$, which equals their separation; the respective NG lateral period is $d = 200 \text{ nm}$. The sample was fixed by a silver paste to a massive copper plate which served as a heat sink and located between the poles of an electromagnetic coil.

B. Time-resolved pump-probe measurements

The pump-probe scheme was realized by means of two mode-locked Erbium-doped ring fiber lasers. The lasers generate pulses of 150 fs duration with the repetition rate of 80 MHz at the wavelengths of 1046 nm (pump pulses) and 780 nm (probe pulses). The pump pulses excited the NG through the GaAs substrate, which is transparent at the pump pulse wavelength. The energy density in the focused pump spot of $5 \mu\text{m}$ diameter was 12 mJ/cm^2 at the substrate backside. The energy density in the $1 \mu\text{m}$ diameter spot of the linearly polarized probe pulse at the NG surface was 1 mJ/cm^2 . The detection of the Kerr rotation of the probe pulse polarization plane was realized in a differential scheme based on a Wollaston prism and a balanced optical receiver with 10-MHz bandwidth. The modulation of the probe pulse intensity was measured by a single photodiode with no polarization optics on the optical path of the probe beam reflected from the sample. The temporal resolution was achieved by means of an asynchronous optical sampling (ASOPS) technique [45]. The pump and probe oscillators were locked with a frequency offset of 800 Hz. In combination with the 80-MHz repetition rate, it allowed measurement of the time-resolved signals in a time window of 12.5 ns with time resolution limited by the probe pulse duration.

C. Modeling the NG phonon modes (spectrum, spatial distribution, excitation and detection)

The coherent elastic response of the NG and its optical detection were modeled using finite element methods by means of COMSOL Multiphysics[®] software (version 5.4) [46]. The list of material parameters used for the calculations with respective references is given

in Supplementary Table 1.

D. Modeling the interaction of three harmonic oscillators

The interaction of the phonon and magnon modes in the NG is described by a model of three interacting oscillators described by the following system of equations:

$$\dot{a}_j + \gamma_j a_j + i\omega_j a_j - i \sum K_{jl} a_l = A_j \delta(t)$$

where a_j are the complex amplitudes ($j = \text{QTA}^*$, QLA or FM) and parameters γ_j , ω_j , and A_j are the damping, frequency and excitation amplitude, respectively. The coupling tensor \hat{K} has the form

$$\hat{K} = \begin{pmatrix} 0 & 0 & \kappa \\ 0 & 0 & \kappa \\ \kappa & \kappa & 0 \end{pmatrix}$$

where the parameter $\kappa = \Delta/2$. Fig. 4b in the main text shows the FFT of $a_{\text{FM}}(t)$ obtained by the analytical solution for the following parameters: $A_{\text{QTA}^*} = 0$, $A_{\text{QLA}} = 10$, $A_{\text{FM}} = 1$, $\omega_{\text{QTA}^*} = 2\pi \times 13.1 \text{ GHz}$, $\omega_{\text{QLA}} = 2\pi \times 14.6 \text{ GHz}$, $\omega_{\text{FM}} = 2\pi \times (7.12 + \alpha B) \text{ GHz}$, where $\alpha = 53 \text{ GHz/T}$; $\gamma_{\text{QTA}^*} = \gamma_{\text{QLA}} = \gamma_{\text{FM}} = \kappa = 2\pi \times 0.2 \text{ GHz}$. The relation $A_{\text{QLA}}/A_{\text{FM}}$ corresponds to the amplitudes and respective energies of the QLA phonon mode and the magnetization precession (in a plain film) excited by the pump pulse. See Supplementary Note 3 for details.

ACKNOWLEDGMENTS

We acknowledge Boris Glavin for his valuable contribution to this work. We are thankful to Mikhail Glazov, Tetiana Linnik and Vitaly Gusev for fruitful discussions. The work was supported by the Bundesministerium für Bildung und Forschung through the project VIP+ "Nanomagneton" and by the Deutsche Forschungsgemeinschaft and the Russian Foundation for Basic Research (Grants No. 19-52-12065 and 19-52-12038) in the frame of the International Collaborative Research Center TRR 160. A.N.P. acknowledges for the partial financial support the Russian President Grant No. MD-5791.2018.2.

IX. AUTHOR CONTRIBUTIONS

F.G. constructed the experimental setup, carried out the experiment and performed the data analysis. A.V.S. and A.V.A. designed the experiment and supervised the experiment and theoretical modeling, S.M.K. designed the nanogratings and performed theoretical analysis and numerical modeling, A.N.P. discussed and modeled the experimental data, D.D.Y. performed the experiment and characterized the nanograting by atomic force microscopy, M. W. deposited the Galfenol films, A. N. produced the nanogratings, A.W.R. designed the Galfenol samples and performed numerical modeling, A.V.S., A.V.A, F.G., S.M.K, A.W.R., D.R.Y, and M.B. discussed the results and wrote the manuscript.

X. COMPETING INTERESTS

The authors declare that they have no competing financial interests.

XI. SUPPLEMENTARY INFORMATION

see below

XII. CORRESPONDENCE

Correspondence and requests for materials should be addressed to Felix Godejohann (email: felix.godejohann@tu-dortmund.de) or Alexey Scherbakov (email: alexey.shcherbakov@tu-dortmund.de).

Supplementary information

Excitation and detection of coherent magnon polarons in a ferromagnetic nanograting

Felix Godejohann,¹ Alexey V. Scherbakov,^{1,2} Serhii M. Kukhtaruk,^{1,3} Alexander
N. Poddubny,² Dmytro D. Yaremkevich,¹ Mu Wang,⁴ Achim Nadzeyka,⁵
Dmitri R. Yakovlev,¹ Andrew W. Rushforth,⁴ Andrey V. Akimov,⁴ and Manfred Bayer¹

¹*Experimentelle Physik 2, Technische Universität Dortmund,
Otto-Hahn-Str. 4a, 44227 Dortmund, Germany.*

²*Ioffe Institute, Politechnicheskaya 26, 194021 St. Petersburg, Russia.*

³*Department of Theoretical Physics,
V.E. Lashkaryov Institute of Semiconductor Physics,
Pr. Nauky 41, 03028 Kyiv, Ukraine.*

⁴*School of Physics and Astronomy, University of Nottingham,
Nottingham NG7 2RD, United Kingdom.*

⁵*Raith GmbH, Konrad-Adenauer-Allee 8, 44263 Dortmund, Germany.*

I. OPTICAL EXCITATION AND DETECTION OF THE ACOUSTIC MODES IN A METALLIC NANOGRATING

In picosecond ultrasonics, pump-probe experiments are used to excite and detect acoustic modes of a solid in the GHz frequency range. In order to describe such an acoustic system, the main equation of linear elasticity is used (see for example Ref. [1]):

$$\rho \frac{\partial^2 u_i}{\partial t^2} = \frac{\partial \sigma_{ij}}{\partial r_j} + \mathcal{F}_i, \quad i, j = x, y, z, \quad (\text{S1})$$

where ρ is the mass density, u_i is the displacement field, $r = (x, y, z)^T$, σ_{ij} are the stress tensor elements and \mathcal{F}_i is an arbitrary external force density. The stress tensor elements are given by Hooke's law:

$$\sigma_{ij} = c_{ijkl} \eta_{kl} \quad (\text{S2})$$

where c_{ijkl} are the stiffness tensor elements and η_{kl} are the strain tensor elements. For a cubic material, it is well known that there are only three different nonzero elements in the stiffness tensor: $c_{xxxx} = c_{11}$, $c_{xxyy} = c_{12}$ and $c_{yzyz} = c_{44}$. For small displacements, the strain tensor elements are derived by

$$\eta_{kl} = \frac{1}{2} \left(\frac{\partial u_k}{\partial r_l} + \frac{\partial u_l}{\partial r_k} \right), \quad k, l = x, y, z. \quad (\text{S3})$$

The external force density, \mathcal{F}_i , depends on the thermal stress tensor elements σ_{ij}^{th} and reads

$$\mathcal{F}_i = \frac{\partial \sigma_{ij}^{\text{th}}}{\partial r_j}. \quad (\text{S4})$$

As it is mentioned in Methods, the pump light has normal incidence to the backside of the structure, i.e. the GaAs/(Fe,Ga) interface. In this case, only the σ_{zz}^{th} component of the thermal stress tensor is nonzero, i.e.

$$\sigma_{zz}^{\text{th}} = -\beta_G C_1 T_1, \quad (\text{S5})$$

where β_G is the Grüneisen parameter, C_1 is the volumetric heat capacity and T_1 is the lattice temperature.

Equations (S1) - (S5) form a total set of equations for the phonon system. Let $n = (n_x, n_y, n_z)^T$ be a unit vector normal to the surface, then the boundary condition for the Galfenol-Air interface can be considered as free ($\sigma_{ij} \cdot n_j = 0$). Additionally, the normal

components of stress have to be continuous at the Galfenol-GaAs interface. Hence, equations (S1), (S4) and (S5) can be explicitly written as

$$\begin{aligned}\rho \frac{\partial^2 u_x}{\partial t^2} &= \frac{\partial \sigma_{xx}}{\partial x} + \frac{\partial \sigma_{xy}}{\partial y} + \frac{\partial \sigma_{xz}}{\partial z} \\ \rho \frac{\partial^2 u_y}{\partial t^2} &= \frac{\partial \sigma_{xy}}{\partial x} + \frac{\partial \sigma_{yy}}{\partial y} + \frac{\partial \sigma_{yz}}{\partial z} \\ \rho \frac{\partial^2 u_z}{\partial t^2} &= \frac{\partial \sigma_{xz}}{\partial x} + \frac{\partial \sigma_{yz}}{\partial y} + \frac{\partial \sigma_{zz}}{\partial z} - \beta_G C_1 \frac{\partial T_1}{\partial z},\end{aligned}\tag{S6}$$

The amplitude of the optically excited phonon mode is proportional to the overlap integral

$$\int \tilde{u}_z \frac{\partial \tilde{T}_1}{\partial z} dV,\tag{S7}$$

where the tilde means similar normalization as it is done in the main text. With respect to the center of the grooves $\frac{\partial \tilde{T}_1}{\partial z}$ is a symmetric function and, therefore, only phonon modes with symmetric \tilde{u}_z or symmetric $\tilde{\eta}_{zz}$ can be excited. Hereafter, symmetric and antisymmetric is always meant with respect to the center of the grooves.

Our main tool for modeling the phonon properties in the nanograting (NG) is COMSOL Multiphysics[®][2]. In order to visualize the time dependence of the spatially resolved displacement and strain, we have implemented the two-temperature model for electrons and the lattice into COMSOL[3–5]. Finally, equations (S1) - (S5) are solved by using the finite element method with COMSOL.

Using the parameters shown in Table 1, time dependent simulations lead to two main excitable phonon modes with frequencies of 13.1 GHz (QTA) and 15.3 GHz (QLA). However, it is known, that for periodic systems Bragg reflections lead to the formation of symmetric and antisymmetric modes with frequencies close to each other[6]. An additional eigenfrequency analysis shows antisymmetric modes with 0.1 GHz smaller frequencies for both already mentioned symmetric modes. However, only the antisymmetric counterpart of the QTA mode, QTA*, will be considered. Due to the symmetry of QTA*, it cannot be excited optically. A careful discussion of the time dependent simulations of the (excitable) QTA and QLA modes is given below.

The magnon-phonon interaction is determined by the normalized spatial profiles of $\tilde{\eta}_{zz}$ and $\tilde{\eta}_{xz}$, which are shown in the main text in Fig. 4a. The normalized strain component, $\tilde{\eta}_{zz}$, which is responsible for the excitation is shown for the QTA* (a), QTA (b), and QLA (c) mode in Fig. S1. By comparing the normalized $\tilde{\eta}_{xx}$ and $\tilde{\eta}_{zz}$ components of the corresponding

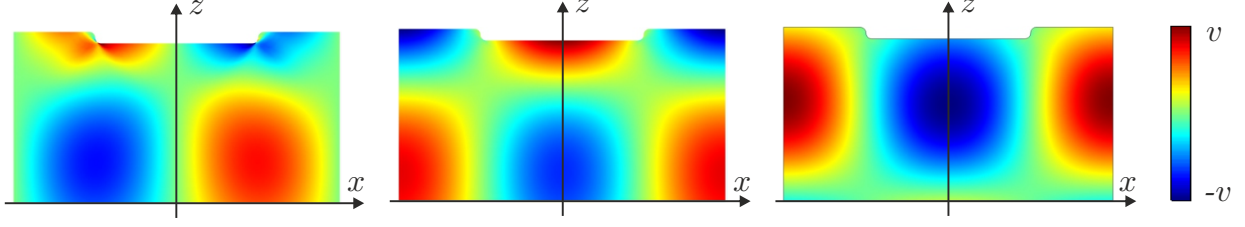


Figure S1. Spatial profiles of the normalized $\tilde{\eta}_{zz}$ component of QTA* (a), QTA (b), and QLA (c) modes. Note that, because of the normalization, the value of v (color scale on the right) is different for different modes. Since the integral of the square of any strain component is equal to one, the actual value of v is not important for the analysis.

modes (see Fig. 4a in the main text), one can see similar spatial distributions, but opposite phases.

The interaction between light and matter is described by Maxwell's equations. If an acoustic wave propagates through a medium, the dielectric permittivity tensor

$$\hat{\epsilon} = \epsilon_0 \hat{\mathbf{I}} + \hat{\epsilon}^{\text{PhE}}, \quad (\text{S8})$$

and, therefore, the optical properties of the medium are periodically modulated. Here, ϵ_0 is the dielectric constant of the unperturbed medium and $\hat{\mathbf{I}}$ the unity tensor. The photo-elastic dielectric permittivity tensor, $\hat{\epsilon}^{\text{PhE}}$, of a cubic material reads

$$\hat{\epsilon}^{\text{PhE}} = -\epsilon_0^2 \begin{pmatrix} p_{11}\eta_{xx} + p_{12}\eta_{yy} + p_{12}\eta_{zz} & 2p_{44}\eta_{xy} & 2p_{44}\eta_{xz} \\ 2p_{44}\eta_{xy} & p_{12}\eta_{xx} + p_{11}\eta_{yy} + p_{12}\eta_{zz} & 2p_{44}\eta_{yz} \\ 2p_{44}\eta_{xz} & 2p_{44}\eta_{yz} & p_{12}\eta_{xx} + p_{12}\eta_{yy} + p_{11}\eta_{zz} \end{pmatrix}, \quad (\text{S9})$$

where $p_{\alpha\beta}$ are the nonzero complex photoelastic constants. Unfortunately, these constants are not yet known for Galfenol, which is the reason why we used them as fitting parameters.

Let us consider the case of a plain film, where the probe light has normal incidence to the surface. Then, the intensity of the reflected probe pulse, $\Delta I(t)$, for the case of an arbitrary polarization in the xy -plane can be described by [5]

$$\Delta I(t) = |r_0 + \delta r_x|^2 + |r_0 + \delta r_y|^2 - 2|r_0|^2, \quad (\text{S10})$$

where $r_0 = \frac{k_0 - k}{k_0 + k}$ is the unperturbed reflection coefficient, $k_0 = \frac{2\pi}{\lambda_0}$ is the wavenumber and λ_0 is the wavelength of light in vacuum, respectively. The wavenumber of light in the medium

is $k = k_0 n$, where n is the refractive index of the medium. The perturbation of reflection, δr_j , can be written as

$$\delta r_j = i \frac{2k_0^3}{(k_0 + k)^2} \int_{-\infty}^h (\varepsilon_{jx}^{\text{PhE}} \cos \psi + \varepsilon_{jy}^{\text{PhE}} \sin \psi) e^{-2ik(z-h)} dz, \quad j = x, y, \quad (\text{S11})$$

where ψ is the angle between the probe polarization and the x -axis. Moreover, the $\varepsilon_{jz}^{\text{PhE}}$ components of the dielectric permittivity do not contribute to the reflectivity signal due to normal incidence of the probe light.

Equations (S10) - (S11) are obtained by considering a Galfenol/Air interface and a small ratio between the skin depth and the film thickness h : $|e^{2ikh}| = 0.002 \ll 1$, where the used parameters can be found in Table 1.

If we now consider a nanograting with depth a , the strain components in equation (S11) depend on, both the x and z coordinate. For the case of shallow grooves ($a \ll h$) equation (S11) can be naively changed by including the average over one period in the x -direction. This results in a new perturbation of reflection

$$\delta r_j^{\text{NG}} = i \frac{2k_0^3}{(k_0 + k)^2 d} \int_{-d/2}^{d/2} \int_{-\infty}^h (\varepsilon_{jx}^{\text{PhE}} \cos \psi + \varepsilon_{jy}^{\text{PhE}} \sin \psi) e^{-2ik(z-h)} dx dz. \quad (\text{S12})$$

By using the Wave Optics module provided by COMSOL, the complete shape of the nanograting (without any approximations) is taken into account. The calculated spectra for p -polarized probe light ($\psi = 0$) can be found in Fig. S2. The solid black line shows the calculated normalized spectrum for the η_{xx} component containing both excited modes. Considering an energy density of 12 mJ/cm^2 for the pump pulse the calculated amplitude of η_{xx} is $4.4 \cdot 10^{-4}$. The red (short dashed) line shows the calculated reflectivity spectrum using equation (S12). It can be seen, that the lower QTA mode is detected, but the upper QLA mode is not. The blue (short dotted) line shows the calculated spectrum considering the NG. In this case, the QLA mode can be detected, but with a much smaller amplitude than for the QTA mode. Figure S2 is calculated for the following fixed photo elastic constants: $-\varepsilon_0^2 p_{11} = 1$, $-\varepsilon_0^2 p_{12} = 1.1 - 1.1i$, and $p_{44} = p_{11} - p_{12}$. Thus, Fig. S2 qualitatively describes the experimental results which is shown in Fig. 1c in the main text. By comparing the calculated spectrum given by equation (S12) and the Wave Optics module, one can conclude that equation (S12) gives a reasonable approximation for a shallow NG.

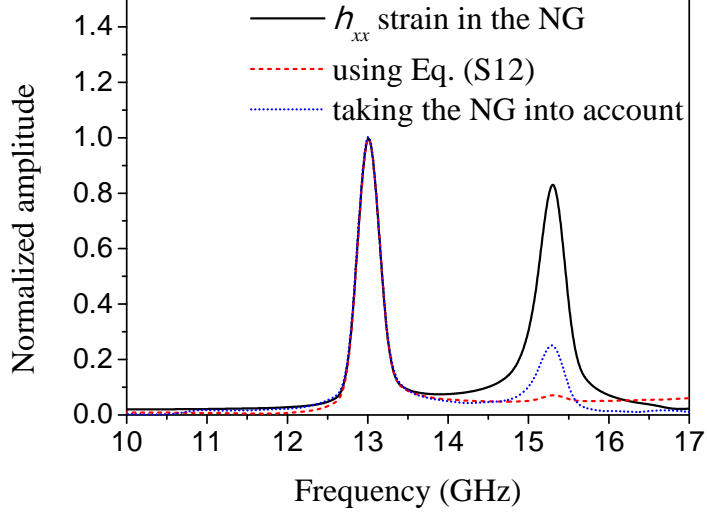


Figure S2. Normalized spectral amplitude of η_{xx} (solid black line) at the spatial coordinate ($x = 0$, $z = h - 2a$). The reflectivity spectrum shown by the red short dashed line has been calculated by equation (S12). The reflectivity spectrum shown by the blue short dotted line has been calculated by the Wave Optics module by taking the shape of the NG into account.

II. MAGNETO-ELASTIC INTERACTION IN BULK FERROMAGNETS

The magneto-elastic interaction for cubic ferromagnets is given by the magneto-elastic free energy

$$F_m^{\text{m-el}} = b_1 (\eta_{xx} m_x^2 + \eta_{yy} m_y^2 + \eta_{zz} m_z^2) + b_2 (\eta_{xy} m_x m_y + \eta_{yz} m_y m_z + \eta_{xz} m_x m_z), \quad (\text{S13})$$

where b_1 and b_2 are the magneto-elastic constants, $m_i = \frac{M_i}{M_s}$ are the components of the magnetization normalized to the saturation magnetization, M_s . In order to describe the coupling between spin waves and phonons[7] one has to add a magneto-elastic term to the external force density introduced in eq. (S4):

$$\mathcal{F}_i^m = \frac{\partial \sigma_{ij}^m}{\partial r_j} \quad (\text{S14})$$

where the magnetic stress tensor, σ_{ij}^m , is given by the free energy density of a ferromagnet, $F_m^{\text{m-el}}$, accordingly to [1]

$$\sigma_{ij}^m = \frac{\partial F_m^{\text{m-el}}}{\partial \eta_{ij}}. \quad (\text{S15})$$

In ferromagnetic structures, the precession of magnetization is usually modeled by the Landau-Lifshitz-Gilbert equation:

$$\frac{\partial \mathbf{m}}{\partial t} = -\gamma \mathbf{m} \times \mathbf{B}_{\text{eff}} + \alpha \mathbf{m} \times \frac{\partial \mathbf{m}}{\partial t} \quad (\text{S16})$$

where γ , \mathbf{B}_{eff} and α are the gyromagnetic ratio, vacuum permeability, effective magnetic field, and the Gilbert damping parameter, respectively. The effective magnetic field is given by

$$\mathbf{B}_{\text{eff}} = -\nabla_m F_m + D\nabla^2 \mathbf{m} \quad (\text{S17})$$

where D is the exchange stiffness constant, $\nabla_m = (\partial/\partial m_x, \partial/\partial m_y, \partial/\partial m_z)^T$, and $\nabla^2 = \partial^2/\partial x^2 + \partial^2/\partial y^2 + \partial^2/\partial z^2$. For a cubic bulk material, the free energy density can be written as

$$F_m = -\mathbf{m} \cdot \mathbf{B} + K_1(m_x^2 m_y^2 + m_y^2 m_z^2 + m_x^2 m_z^2) + F_m^{\text{m-el}} \quad (\text{S18})$$

where \mathbf{B} is an external magnetic field and K_1 is the cubic anisotropy coefficient.

Equations (S1) - (S3) and (S13) - (S18) are the main set of nonlinear equations to describe the magneto-elastic interaction. For further analysis, the external magnetic field, \mathbf{B} , is applied in the xy -plane along the [110]-crystallographic direction. Moreover, the cubic anisotropy term in (S18) is neglected for the sake of simplicity. In order to derive the dispersion relation for the coupled spin waves with phonons, the main set of equations has to be linearized, so that the zero points of the resulting determinant lead to the dispersion relation

$$\begin{aligned} & (\omega^2 - v_l^2 k^2 + i\omega\gamma_0)(\omega^2 - v_t^2 k^2 + i\omega\gamma_0)(\omega^2 - S^2) - \\ & S(\omega^2 - v_t^2 k^2 + i\omega\gamma_0)\bar{\beta}_1 k^2 - S(\omega^2 - v_l^2 k^2 + i\omega\gamma_0)\bar{\beta}_2 k^2 - \bar{\beta}_1 \bar{\beta}_2 k^4 = 0 \end{aligned} \quad (\text{S19})$$

where v_l and v_t are the longitudinal (LA) and transversal (TA) sound velocities, γ_0 is a phenomenological damping constant of the lattice, $S = \gamma B + \gamma D k^2 - i\alpha\omega$ gives the frequency and damping of spin waves in the bulk. The relations between $\bar{\beta}_1 = \gamma M_s b_1^2 / (\rho\mu_0)$ and $\bar{\beta}_2 = \gamma M_s b_2^2 / (8\rho\mu_0)$, where μ_0 is the vacuum permeability, and β_1 and β_2 , which are introduced in the main text in equation (1), are defined by: $\beta_1 = \sqrt{\bar{\beta}_1} \omega_r / v_l \approx 0.88$ GHz, and $\beta_2 = \sqrt{\bar{\beta}_2} \omega_r / v_t \approx 0.27$ GHz (see Table 1 below). Here ω_r is the resonance frequency of the uncoupled spin wave-phonon system; it corresponds to crossing points in Fig. 1e in the main text.

III. A MODEL OF THREE COUPLED OSCILLATORS

In Ref. [8], the authors have shown that for each component of the dynamic magnetization and displacement (strain) the problem of the coupled magnon-phonon system can be reduced

to the equations of simple coupled oscillators. Basically, the strength of interaction is given by the overlap integral between the considered phonon and magnon modes. Therefore, we have simplified the magnon-phonon interaction given by the QTA*, QLA and FM modes to a system of three coupled oscillators. We have assumed that there is no interaction between the QTA* and QLA (phonon) modes. In this case the system of equations is the following:

$$\dot{a}_j + \gamma_j a_j + i\omega_j a_j - i \sum_l K_{jl} a_l = A_j \delta(t), \quad (\text{S20})$$

where index j stands for the considered oscillators QTA*, QLA, and FM. The parameters γ_j , ω_j , and A_j are the corresponding damping, frequency and excitation amplitude of each oscillator, respectively; a_j are the unknown complex amplitudes of the eigenmodes. For the mentioned system the coupling tensor, \hat{K} , reads

$$\hat{K} = \begin{pmatrix} 0 & 0 & \kappa \\ 0 & 0 & \kappa \\ \kappa & \kappa & 0 \end{pmatrix}, \quad (\text{S21})$$

where the parameter $\kappa = \Delta/2$. The coupling strength, κ , has been introduced in the main text in equation (1). The introduced parameters $\gamma_j, \omega_j, \kappa$ have the dimension of frequency. For the excitation amplitude in equation (S20) we have considered δ -excitations, because the pump pulse duration is much shorter than the lifetime of the eigenmodes. Then, equations (S20) - (S21) can be easily solved analytically. The Fourier components, $a_j(\omega)$, read

$$a_j(\omega) = \frac{N_j(\omega)}{D(\omega)}, \quad (\text{S22})$$

where, we denote

$$\begin{aligned} N_{\text{QTA}^*}(\omega) &= iA_{\text{QTA}^*} [(\omega + i\gamma_{\text{QLA}} - \omega_{\text{QLA}})(\omega + i\gamma_{\text{FM}} - \omega_{\text{FM}}) - \kappa^2] \\ &\quad + iA_{\text{QLA}}\kappa^2 - iA_{\text{FM}}\kappa(\omega + i\gamma_{\text{QLA}} - \omega_{\text{QLA}}); \\ N_{\text{QLA}}(\omega) &= iA_{\text{QLA}} [(\omega + i\gamma_{\text{QTA}^*} - \omega_{\text{QTA}^*})(\omega + i\gamma_{\text{FM}} - \omega_{\text{FM}}) - \kappa^2] \\ &\quad + iA_{\text{QTA}^*}\kappa^2 - iA_{\text{FM}}\kappa(\omega + i\gamma_{\text{QTA}^*} - \omega_{\text{QTA}^*}); \end{aligned}$$

$$\begin{aligned}
N_{\text{FM}}(\omega) &= iA_{\text{FM}}(\omega + i\gamma_{\text{QTA}^*} - \omega_{\text{QTA}^*})(\omega + i\gamma_{\text{QLA}} - \omega_{\text{QLA}}) \\
&\quad - iA_{\text{QTA}^*}\kappa(\omega + i\gamma_{\text{QLA}} - \omega_{\text{QLA}}) - iA_{\text{QLA}}\kappa(\omega + i\gamma_{\text{QTA}^*} - \omega_{\text{QTA}^*}); \\
D(\omega) &= (\omega + i\gamma_{\text{QTA}^*} - \omega_{\text{QTA}^*})(\omega + i\gamma_{\text{QLA}} - \omega_{\text{QLA}})(\omega + i\gamma_{\text{FM}} - \omega_{\text{FM}}) \\
&\quad - \kappa^2(\omega + i\gamma_{\text{QTA}^*} - \omega_{\text{QTA}^*}) - \kappa^2(\omega + i\gamma_{\text{QLA}} - \omega_{\text{QLA}}).
\end{aligned}$$

The zero points of $D(\omega)$ indicate the eigenfrequencies of the coupled modes. While the frequencies of the phonon modes, $\omega_{\text{QTA}^*} = 2\pi \times 13.0$ GHz and $\omega_{\text{QLA}} = 2\pi \times 14.6$ GHz, do not depend on the magnetic field, the FM frequency, $\omega_{\text{FM}} = 2\pi(7.12 + \alpha B)$ GHz, linearly depends on the magnetic field ($\alpha = 53$ GHz/T). The values correspond to Fig. 2a in the main text.

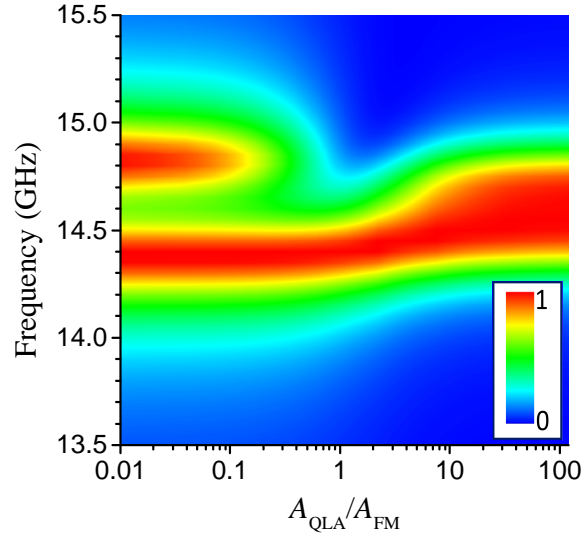


Figure S3. Color map of the normalized amplitude $|a_{\text{FM}}(\omega)|^2$ of the FM mode. Note, that $|a_{\text{FM}}(\omega)|^2$ is normalized to its maximum value for each $A_{\text{QLA}}/A_{\text{FM}}$ for better visualization.

In order to describe the different manifestations of coupling for the QTA* and the QLA mode with the FM mode, the excitation amplitudes have to be considered. In general, the excitation amplitudes are complex. Physically, this means that the oscillators can be excited with different phase ratio. Mainly the manifestation of coupling is determined by the ratio of the excitation amplitudes of two coupled oscillators. In Fig. S3 an example is given, where the normalized amplitude $|a_{\text{FM}}(\omega)|^2$ of the QLA-FM resonance is shown as a function of the relation between the excitation amplitudes, $A_{\text{QLA}}/A_{\text{FM}}$. Here, the excitation amplitudes are assumed to be real and the damping parameters are fixed to $\gamma_{\text{QLA}} = \gamma_{\text{FM}} = \kappa = 2\pi \times 0.2$ GHz. One can conclude from Fig. S3 that for $A_{\text{QLA}}/A_{\text{FM}} < 1$ a well pronounced avoided crossing

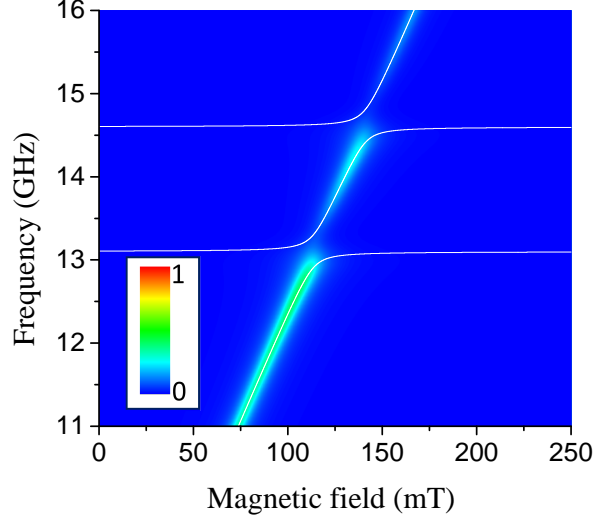


Figure S4. Color map of the normalized amplitude $|a_{\text{FM}}(\omega)|^2$ of the FM mode for the parameters given by Set I.

is observed, whereas for $A_{\text{QLA}}/A_{\text{FM}} > 1$ the avoided crossing is masked by the driving effect.

In the experiment for the lower resonance an avoided crossing without any driving is observed (see Fig. 2a in the main text). This behavior is the result of two coupled oscillators, where one oscillator is excited (FM mode) and the other oscillator is not excited (QTA* mode), because of its symmetry (as it is mentioned in the main text). Using a "proof by contradiction", we will show the validity of the latter statement by discussing the relations of the excitation amplitudes, A_j/A_{FM} .

Let us assume that the lower resonance corresponds to the FM-QTA coupling (**not** FM-QTA*) and the upper one corresponds to the FM-QLA coupling. Then, we know from Fig. S2, that both acoustic modes have similar excitation amplitudes ($A_{\text{QTA}} \approx A_{\text{FM}}$). Therefore, there are three possible relations between the phonon and magnon excitation amplitudes: (I) all modes are equally excited, i.e. $A_{\text{QTA}} = A_{\text{QLA}} = A_{\text{FM}}$, (II) the phonons are excited more strongly than the magnons, i.e. $A_{\text{QTA}} = A_{\text{QLA}} > A_{\text{FM}}$, and (III) the phonons are excited less strongly than the magnons, i.e. $A_{\text{QTA}} = A_{\text{QLA}} < A_{\text{FM}}$.

Here we demonstrate every scenario starting from case (I), i.e. $A_{\text{QTA}} = A_{\text{QLA}} = A_{\text{FM}}$. Fig. S4 shows the square of the absolute value of the FM mode $|a_{\text{FM}}(\omega)|^2$, where the corresponding set of parameters, Set I, reads: $A_{\text{QTA}} = 1, A_{\text{QLA}} = 1, A_{\text{FM}} = 1$, and $\omega_{\text{QTA}} = 2\pi \times 13.1$ GHz, $\omega_{\text{QLA}} = 2\pi \times 14.6$ GHz, $\gamma_{\text{QTA}^*} = \gamma_{\text{QLA}} = \gamma_{\text{FM}} = \kappa = 2\pi \times 0.2$ GHz. In Fig. S4, one can see

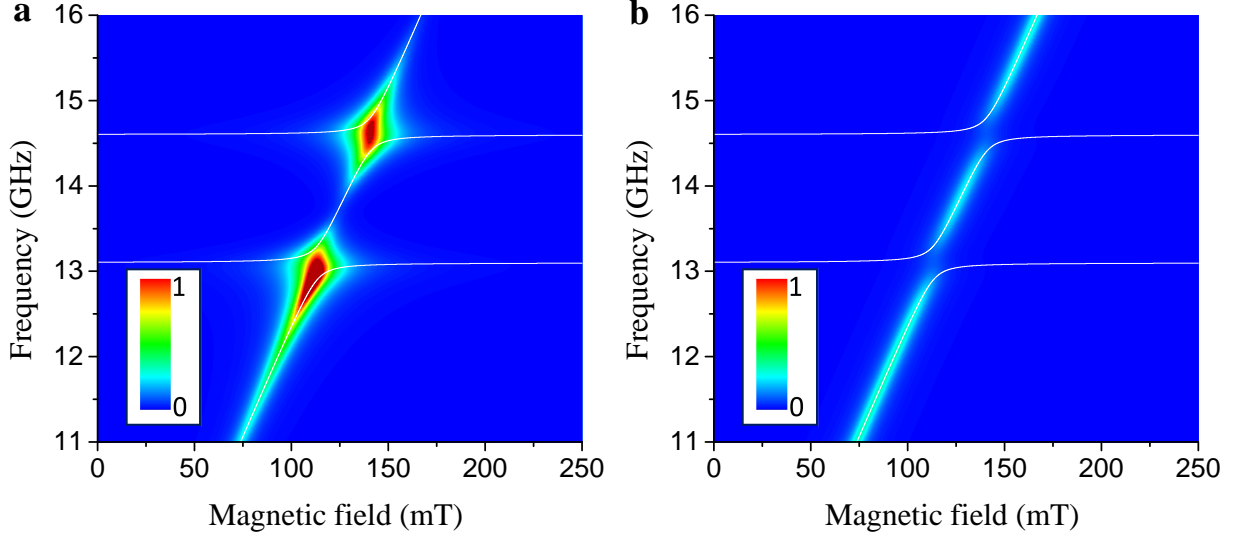


Figure S5. Color map of the normalized amplitude $|a_{\text{FM}}(\omega)|^2$ of the FM mode for the parameters given by **a** Set II and **b** Set III.

avoided crossings for both resonances without any driving effect. However, this scenario is not observed in the experiment for the upper mode (see Fig. 2a in the main text).

Figure S5a shows $|a_{\text{FM}}(\omega)|^2$ for case (II), i.e. $A_{\text{QTA}} = A_{\text{QLA}} > A_{\text{FM}}$, where the corresponding set of parameters, Set II, is the same as Set I except that $A_{\text{QTA}} = 10$ and $A_{\text{QLA}} = 10$. In Fig. S5a, one can see that both strongly excited phonon modes drive the magnon mode. However, this is not observed in the experiment for the lower mode (see Fig. 2a in the main text).

Now, let us consider case (III), i.e. $A_{\text{QTA}} = A_{\text{QLA}} < A_{\text{FM}}$. This scenario is shown in Fig. S5b, where the corresponding set of parameters, set III, is the same as Set I except that $A_{\text{QTA}} = 0.1$ and $A_{\text{QLA}} = 0.1$. As one can see, this does not describe the experimental results, either. Therefore, there has to be a lower phonon mode with a very small or zero excitation amplitude (for anticrossing) and an upper phonon mode with a large excitation amplitude (for driving) compared to the excitation amplitude of the FM mode. The latter case is true for the QLA mode, as it has been already mentioned. The case of a small excitation amplitude of a phonon mode with a close frequency to the QTA mode is realized by introducing its antisymmetric counterpart, QTA^* , with a 0.1 GHz smaller frequency and zero excitation amplitude. This scenario is shown in Fig. 4b in the main text where $A_{\text{QTA}^*} = 0$, $A_{\text{QLA}} = 10$ and all other parameters are the same as for Set I. Compared to the experimental results shown in Fig. 2a the mentioned concept gives a good qualitative agreement. Thus,

we have shown that the antisymmetric QTA* mode is crucially important for the explanation of the main experimental results.

IV. TABLE WITH USED PARAMETERS

Table 1

Acoustic parameters					
	c_{11} , GPa	c_{12} , GPa	c_{44} , GPa	ρ , kg/m ³	Citation
Fe _{0.81} Ga _{0.19}	209*	141*	113*	7800	[9]
GaAs	119	53.8	59.5	5316	[10]
AlAs	119.9	57.5	56.6	3760	[10]
Optical parameters: pump light					
λ_0 , nm	n_{GaAs}	n_{FeGa}			Citation
1046	3.4805	$3.2196 + i \cdot 4.2740$			[11, 12]
Optical parameters: probe light					
λ_0 , nm	n_{GaAs}	n_{FeGa}	$-\varepsilon_0^2 p_{11}$	$-\varepsilon_0^2 p_{12}$	Citation
760	$3.7137 + i \cdot 0.097862$	$2.9688 + i \cdot 3.5337$	1**	$1.1 - i \cdot 1.1^{**}$	[11, 12]
Ferromagnetic parameters of Fe _{0.81} Ga _{0.19}					
M_s , T	K_1 , T	D , T · m ²	b_1 , T	b_2 , T	Citation
1.59	0.023*	$2.4 \times 10^{-17}{}^{***}$	-7.0	-4.7	[13, 14]

*parameters were slightly adjusted to describe the experiment ($\approx 10\%$).

**parameters were fitted to describe the experiment

***note that $D = 2A_{ex}$ from [14].

-
- [1] Tucker, J. W. & Rampton, V. *Microwave ultrasonics in solid state physics* (North-Holland Pub. Co, 1972).
- [2] COMSOL Multiphysics[®] v. 5.4. <http://www.comsol.com>. COMSOL AB, Stockholm, Sweden.
- [3] Anisimov, S. I., Kapeliovich, B. L. & Perel'man, T. L. Electron emission from metal surfaces exposed to ultrashort laser pulses. *Sov. Phys. JETP* **39**, 375 (1974).
- [4] Tas, G. & Maris, H. J. Electron diffusion in metals studied by picosecond ultrasonics. *Phys. Rev. B* **49**, 15046–15054 (1994).

- [5] Thomsen, C., Grahn, H. T., Maris, H. J. & Tauc, J. Surface generation and detection of phonons by picosecond light pulses. *Phys. Rev. B* **34**, 4129–4138 (1986).
- [6] Sadhu, J., Lee, J. H. & Sinha, S. Frequency shift and attenuation of hypersonic surface acoustic phonons under metallic gratings. *Phys. Rev. Lett.* **97**, 133106 (2010).
- [7] Akhiezer, A. I., Bar’iakhtar, V. G. & Peletminskii, S. V. Coupled magnetoelastic waves in ferromagnetic media and ferroacoustic resonance. *Sov. Phys. JETP* **35**, 157–164 (1959).
- [8] Verba, R., Lisenkov, I., Krivorotov, I., Tiberkevich, V. & Slavin, A. Nonreciprocal surface acoustic waves in multilayers with magnetoelastic and interfacial Dzyaloshinskii-Moriya interactions. *Phys. Rev. Applied* **9**, 064014 (2018).
- [9] Clark, A. E. *et al.* Extraordinary magnetoelasticity and lattice softening in bcc Fe-Ga alloys. *J. Appl. Phys.* **93**, 8621–8623 (2003).
- [10] Madelung, O. *Semiconductors: Data Handbook* (Springer, 2004).
- [11] Ordal, M. A., Bell, R. J., Alexander, R. W., Newquist, L. A. & Querry, M. R. Optical properties of Al, Fe, Ti, Ta, W, and Mo at submillimeter wavelengths. *Appl. Opt.* **27**, 1203 (1988).
- [12] Skauli, T. *et al.* Improved dispersion relations for GaAs and applications to nonlinear optics. *J. Appl. Phys.* **94**, 6447–6455 (2003).
- [13] Restorff, J. B. *et al.* Tetragonal magnetostriction and magnetoelastic coupling in Fe-Al, Fe-Ga, Fe-Ge, Fe-Si, Fe-Ga-Al, and Fe-Ga-Ge alloys. *J. Appl. Phys.* **111**, 023905 (2012).
- [14] Gopman, D. B., Sampath, V., Ahmad, H., Bandyopadhyay, S. & Atulasimha, J. Static and dynamic magnetic properties of sputtered Fe-Ga thin films. *IEEE Trans. Mag.* **53**, 1–4 (2017).